

## Low frequency interference between short synchrotron radiation sources

F. Méot,<sup>1,\*</sup> L. Ponce,<sup>2,†</sup> and N. Ponthieu<sup>3</sup>

<sup>1</sup>CEA DSM/DAPNIA/SEA, 91191 Saclay, France

<sup>2</sup>CERN SL/BI, 1211 Geneva 23, Switzerland

<sup>3</sup>ISN, Service d'astrophysique, 38026 Grenoble cedex, France

(Received 23 June 1999; revised manuscript received 19 January 2001; published 7 June 2001)

A recently developed analytical formalism describing low frequency far-field synchrotron radiation (SR) is applied to the calculation of spectral angular radiation densities from interfering short sources (edge, short magnet). This is illustrated by analytical calculation of synchrotron radiation from various assemblies of short dipoles, including an “isolated” highest density infrared SR source.

DOI: 10.1103/PhysRevSTAB.4.062801

PACS numbers: 41.60.-m, 41.85.Ew, 41.75.Ht

### I. INTRODUCTION

Electron and proton synchrotron radiation (SR) interference has long been subject to investigations (see, for instance, [1,2]). Yet, considering the lasting interest in SR for such a purpose as beam diagnostics in electron and TeV-range proton installations [3,4], or for infrared production [5], enriched insight in interference phenomena in the low frequency range and their understanding remain of interest.

In this paper we revisit the subject with recently developed analytical material modeling low frequency SR [6,7] that allows detailed calculation of interference effects. This is illustrated with various assemblies of interfering short sources—possibly subject to earlier more or less detailed publications as will be discussed.

Calculation of coherence times is discussed in Appendix A. Comparisons in Appendixes B and C with accurate numerical simulations based on ray tracing show the efficiency of the method.

### II. LOW FREQUENCY SR MODEL

Regular conditions of SR observation are assumed as follows. An observer located at large distance  $r(t')$  from a particle with angular velocity  $\omega_0 t'$  radiating at time  $t'$  in the direction  $\vec{n}(\phi, \psi)$  (Fig. 1) receives an electromagnetic wave  $[\vec{E}(t), \vec{B}(t) = \vec{n} \times \vec{E}(t)/c]$  at retarded time  $t = t' + \vec{r}(t')/c$ . In what follows the particle time origin  $t' = 0$  coincides with observation direction  $\phi = 0$ . The energy density is given by

$$\frac{\partial^3 W}{\partial \phi \partial \psi \partial \omega} = 2\epsilon_0 c r^2 |\tilde{\vec{E}}(\phi, \psi, \omega)|^2 \quad (1)$$

wherein  $\tilde{\vec{E}}(\phi, \psi, \omega) = \int \vec{E}(\phi, \psi, t) e^{-i\omega t} dt / \sqrt{2\pi}$  is the Fourier transform of  $\vec{E}(\phi, \psi, t)$ ,  $\omega$  is the observed fre-

quency, and  $r$  is assumed constant following classical hypothesis [8]. The low frequency SR approximation is concerned with SR signals  $\vec{E}(\phi, \psi, t)$  with duration  $\Delta T$  that satisfies  $\omega \Delta T \ll 1$ , so that in the series expansion

$$e^{-i\omega t} = 1 - i\omega t - (\omega t)^2/2 - i(\omega t)^3/6 + \dots \quad (2)$$

of the exponential argument in the Fourier transform above one only retains the zeroth order term; in other words, that leads to considering the limit case

$$\begin{aligned} \sqrt{2\pi} \tilde{\vec{E}}(\phi, \psi, t) &= \lim_{\omega \rightarrow 0} \int_{\Delta T} \vec{E}(\phi, \psi, t) e^{-i\omega t} dt \\ &= \int_{\Delta T} \vec{E}(\phi, \psi, t) dt \end{aligned} \quad (3)$$

and identifying the Fourier transform of the signal with its time integral (apart from the  $1/\sqrt{2\pi}$  factor) with the consequences that, on the one hand, the spectrum is white ( $\omega$  independent), and, on the other hand, it is nonzero as long as  $\int \vec{E}(\phi, \psi, t) dt$  is not null.

By considering SR over a finite trajectory arc  $\pm\alpha/2$ , one can write (Appendix A)

$$\Delta T = \frac{L}{2\gamma^2 c} [1 + \gamma^2(\phi^2 + \psi^2) + K^2/3] \quad (4)$$

( $L = \rho\alpha$  is the arc length with  $\rho$  being the curvature radius,  $K = \alpha\gamma/2$  is the deflection parameter,  $\gamma$  is the Lorentz relativistic factor); considering, in addition, that most of the radiated energy is contained within  $\gamma^2(\phi^2 + \psi^2) < 1 + K^2$  [see Eq. (10)] that leads, in particular, to the upper frequency validity limit

$$\omega_{\text{limit}} \approx \omega_c / [3K(1 + K^2)] \quad (5)$$

( $\omega_c = 3\gamma^3 c / 2\rho$  is the usual critical frequency). Note that the far-field hypothesis sets a lower frequency validity limit approximately  $\omega > \gamma^2 c / r$  (conversely the near-field component in  $\vec{E}$  would need to be accounted for if  $r$  were less than  $\gamma^2 c / \omega$ ) [5]; in addition, we assume a sharp edge field model at magnet ends located at  $\pm\alpha/2$ , which is

\*Email address: fmeot@cea.fr

†Email address: laurette.ponce@cern.ch.

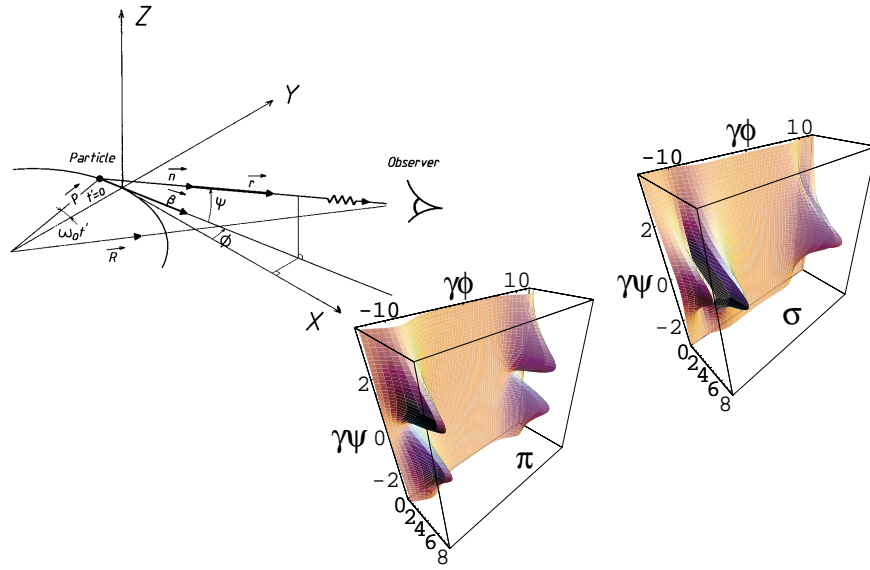


FIG. 1. (Color) Reference laboratory frame and notations used in the text and, on the right,  $\sigma$  and  $\pi$  polarization components of the angular distribution the observer typically sees at infinite distance, given trajectory arc  $-10/\gamma < \alpha < 10/\gamma$  [Eq. (9) with  $K = 10$ ]. Both distributions renormalized to the  $\sigma$  density in the forward direction ( $\sigma = 0, \psi = 0$ ) for further comparisons.

justified as to our concern since the shape of end field falloffs does not affect the energy density in the range  $\omega < \omega_{\text{limit}}$  [6,9].

It has been shown [6] that the electric signal can be written under the form

$$E_{\sigma}(t') = \frac{q\omega_0\gamma^4}{\pi\epsilon_0cr} \frac{(1 + \gamma^2\psi^2) - \gamma^2(\omega_0t' - \phi)^2}{[1 + \gamma^2\psi^2 + \gamma^2(\omega_0t' - \phi)^2]^3} \text{rect}(t'/2T'),$$

$$E_{\pi}(t') = \frac{q\omega_0\gamma^4}{\pi\epsilon_0cr} \frac{-2\gamma\psi\gamma(\omega_0t' - \phi)}{[1 + \gamma^2\psi^2 + \gamma^2(\omega_0t' - \phi)^2]^3} \text{rect}(t'/2T'),$$
(6)

in particle time or, after notations introduced in Ref. [8], under the form

$$E_{\sigma}(\phi, \psi, t) = \frac{q\omega_0\gamma^4}{\pi\epsilon_0cr} \frac{1 - 4\sinh^2[\frac{1}{3}\sinh^{-1}u(\phi, \psi, t)]}{(1 + \gamma^2\psi^2)^2\{1 + 4\sinh^2[\frac{1}{3}\sinh^{-1}u(\phi, \psi, t)]\}^3} \text{rect}[t/2T(\phi, \psi)],$$

$$E_{\pi}(\phi, \psi, t) = \frac{q\omega_0\gamma^4}{\pi\epsilon_0cr} \frac{4\gamma\psi\sinh[\frac{1}{3}\sinh^{-1}u(\phi, \psi, t)]}{(1 + \gamma^2\psi^2)^{5/2}\{1 + 4\sinh^2[\frac{1}{3}\sinh^{-1}u(\phi, \psi, t)]\}^3} \text{rect}[t/2T(\phi, \psi)]$$
(7)

in observer time (the rectangle function  $\text{rect}(x) = 1$  if  $-1/2 < x < 1/2$  defines the limited time support of the signal;  $2cT' = \rho\alpha$  is the trajectory arc length and  $2cT(\phi, \psi)$  is its observation dependent Lorentz transform;  $u = \frac{1}{2}[\gamma\phi/(\sqrt{1 + \gamma^2\psi^2})](3 + \frac{\gamma^2\phi^2}{1 + \gamma^2\psi^2}) - 2\frac{\omega_c}{(1 + \gamma^2\psi^2)^{3/2}}t$ . Integration of Eq. (6) in particle time is easier than the integration of the observer time expression of Eq. (7) and straightforwardly leads to the approximate Fourier transform

$$\tilde{E}_{\sigma}(\phi, \psi, \omega) = \frac{q\gamma}{(2\pi)^{3/2}\epsilon_0cr} \left( \frac{K - \gamma\phi}{1 + (K - \gamma\phi)^2 + \gamma^2\psi^2} + \frac{K + \gamma\phi}{1 + (K + \gamma\phi)^2 + \gamma^2\psi^2} \right),$$

$$\tilde{E}_{\pi}(\phi, \psi, \omega) = \frac{q\gamma}{(2\pi)^{3/2}\epsilon_0cr} \gamma\psi \left( \frac{1}{1 + (K - \gamma\phi)^2 + \gamma^2\psi^2} - \frac{1}{1 + (K + \gamma\phi)^2 + \gamma^2\psi^2} \right),$$
(8)

where the index  $\sigma$  designates the polarization component parallel to the bend plane and orthogonal to the propagation direction  $\vec{n}$ , and the index  $\pi$  designates the polarization component normal to  $\vec{E}_{\sigma}$  and  $\vec{n}$ . By introducing Eq. (8) into Eq. (1) the spectral angular energy density ensues (shown in Fig. 1)

$$\begin{aligned}\frac{\partial^3 W_\sigma}{\partial \phi \partial \psi \partial \omega} &= \frac{q^2 \gamma^2}{4\pi^3 \epsilon_0 c} \left( \frac{K - \gamma \phi}{1 + (K - \gamma \phi)^2 + \gamma^2 \psi^2} + \frac{K + \gamma \phi}{1 + (K + \gamma \phi)^2 + \gamma^2 \psi^2} \right)^2, \\ \frac{\partial^3 W_\pi}{\partial \phi \partial \psi \partial \omega} &= \frac{q^2 \gamma^2}{4\pi^3 \epsilon_0 c} \gamma^2 \psi^2 \left( \frac{1}{1 + (K - \gamma \phi)^2 + \gamma^2 \psi^2} - \frac{1}{1 + (K + \gamma \phi)^2 + \gamma^2 \psi^2} \right)^2.\end{aligned}\quad (9)$$

Some useful comments arise (see Ref. [6] for more details). The  $\sigma$  and  $\pi$  end peaks of edge SR are in directions  $(\gamma \phi, \gamma \psi)_{\sigma\text{-peak}} \stackrel{|K| \geq \sqrt{3}}{\approx} (\pm \sqrt{1 + K^2} \pm 2\sqrt{1 + K^2}, 0) \stackrel{K \gg 1}{\approx} [\pm(K \pm 1), 0]$  and  $(\gamma \phi, \gamma \psi)_{\pi\text{-peak}} = \{\pm[(1 + K^2)/(\sqrt{2 + K^2})], \pm[(1 + K^2)/(2 + K^2)]\} \stackrel{K \gg 1}{\approx} (\pm K, \pm 1)$ , that is to say about  $\pm 1/\gamma$  from the particle entrance or exit directions; they take their source within about  $(2/\gamma)$  trajectory arc at dipole ends, while low frequency SR from beyond this range has negligible intensity<sup>1</sup>; the  $\sigma$  peaks merge into a single, central one if  $|K| < \sqrt{3}$  and energy densities [Eq. (9)] tend towards “short magnet” SR, close in its shape to the  $K \ll 1$  limit instantaneous SR. The  $\sigma$  and  $\pi$  rms aperture values of Eq. (9) distributions are

$$\begin{aligned}\gamma \phi_{\text{rms}}|_{\psi=0} &= \gamma \psi_{\text{rms}}|_{\phi=0} \\ &= \sqrt{1 + K^2} \rightarrow \begin{cases} K & \text{if } K \gg 1, \\ 1 & \text{if } K \ll 1, \end{cases}\end{aligned}\quad (10)$$

featuring expected values for  $K \gg 1$  and for  $K \ll 1$  [8]. Integration of Eq. (9) shows that the  $\pm 2$ -rms aperture encompasses about 90% of the radiated energy. From a practical viewpoint the low frequency model is correct within a few percent over a few rms aperture, up to about the  $\omega_{\text{limit}}$ .

### III. INTERFERING SHORT SOURCES

Our working hypothesis is as follows. In the sequel neighboring short sources are considered that radiate impulse of the form

$${}^N E_{\sigma,\pi}(\phi, \psi, t) = \sum_{i=1}^N \delta(t + T_i) * E_{i\sigma,\pi}(\phi, \psi, t), \quad (11)$$

wherein  $*$  denotes the convolution product,  $\delta$  is the Dirac distribution,  $N$  is the number of sources that have individual contributions  $E_{i\sigma,\pi}$  and are spaced by observer time intervals  $T_i$ ; these depend on the observer direction  $(\phi, \psi)$  (Fig. 1) and combine, on the one hand, magnet traversal delays that can be approximated by Eq. (4) to second order in  $1/\gamma$  and, on the other hand, straight section traversals

$$\Delta T_d = \frac{d}{2\gamma^2 c} (1 + \gamma^2 \theta^2) \quad (12)$$

with  $\theta$  being the observation angle with respect to particle velocity, the expression of which in terms of the observer direction  $(\phi, \psi)$  is problem dependent and will be discussed later.

<sup>1</sup>The ratio of body to edge  $\sigma$ -component SR from a strong dipole ( $K \gg 1$ ) is  $[\Gamma^2(2/3)/2^{1/3}](\omega/\omega_c)^{2/3}:(1 + 1/K)^2/2$  in favor of edge SR since  $\omega \ll \omega_c$  [Eq. (5)].

In the *short* SR source approximation ( $L \ll d$ ) the Fourier transform of the time impulse [Eq. (11)] leads to the amplitude density

$${}^N \tilde{E}_{\sigma,\pi}(\phi, \psi, \omega) = \sum_{i=1}^N e^{i\omega T_i} \tilde{E}_{i\sigma,\pi}(\phi, \psi, \omega) \quad (13)$$

whose modulus square provides the spectral angular energy density.

As to our concern, writing the interference under this form has the merit of showing that possible further low frequency approximation does not concern the phase term  $e^{i\omega T_i}$  which is the exact Fourier transform of the  $\delta$  factor, entailing that the upper frequency validity limit [Eq. (5)] is independent of the lags  $\Delta T_i = T_i - T_{i-1}$  and depends only on the individual magnetic lengths of the sources. This is no longer true if the short source condition  $\Delta T \ll \Delta T_i$  is not fulfilled, that is to say, if the phase  $\omega \Delta T$  of the signal is of the order of magnitude of the phase advance  $\omega \Delta T_i$  from one source to the next; in such a case, higher order terms in Eq. (2) need in principle be retained. However the validity of the zeroth order approximation of Eq. (3) may still be good as discussed in Sec. III A, whereas for illustration higher order approximation is briefly addressed in Appendix C in the conditions of the CERN Large Hadron Collider (LHC) at injection energy ranges (450 GeV protons) [10,11].

#### A. Short dipoles at the Large Electron-Positron Collider, 20 GeV leptons

Various numerical simulations and experimental measurements relevant to low frequency SR interference have been reported regarding a diagnostic miniwiggler installed at the Large Electron-Positron Collider (LEP) for 3D bunch profile measurements [12] that could be operated as a single- to four-dipole assembly. Interference could be observed in some configurations of the short dipole series that caused a strong attenuation of visible SR compared to what was delivered by a single dipole; this has been subject to extensive intensity and spectrum measurements [13,14] as well as detailed numerical simulations [based on numerical calculation of  $\vec{E}(\phi, \psi, t)$  and of its Fourier transform  $\tilde{\vec{E}}(\phi, \psi, \omega)$ ] of two-, three-, or four-dipole interference [15] that confirmed the observations (see, for instance, [13], Fig. 3). However those numerical simulations can be fully reproduced from the analytical low frequency SR model developed here, as follows.

We consider for simplicity a two-dipole geometry of the former LEP miniwiggler [13] that delivers an electric field impulse doublet of the form

$${}^{11}E_{\sigma,\pi}(\phi, \psi, t) = [\delta(-t - T/2) - \delta(t - T/2)] * E_{\sigma,\pi}(\phi, \psi, t) \quad (14)$$

as schemed in Fig. 2 [Eqs. (7) and (11) with  $N = 2$ ,  $E_{1\sigma,\pi}(\phi, \psi, -t) = -E_{2\sigma,\pi}(\phi, \psi, t) = E_{\sigma,\pi}(\phi, \psi, t)$  and  $T_1 = -T_2 = T/2$ ], an odd function of time what-

ever  $(\phi, \psi)$ , and with total duration  $2\Delta T + \Delta T_d |\theta^2 = (\phi - K/\gamma)^2 + \psi^2|$  with  $\Delta T$  from Eq. (4) and  $\Delta T_d$  from Eq. (12) taken for  $\theta^2 = (\phi - K/\gamma)^2 + \psi^2$  according to the frame defined in Fig. 2. By taking time and  $\phi$ -angle origins for single impulses  $E_{1\sigma,\pi}$  and  $E_{2\sigma,\pi}$  at the center of, respectively, the left dipole and the right dipole the coherence time writes (see Appendix A)

$$T = \frac{1}{2} \Delta T|_{K=K/2, \phi=\phi+K/2\gamma} + \Delta T_d|_{\theta^2=(\phi+K/\gamma)^2+\psi^2} + \frac{1}{2} \Delta T|_{K=-K/2, \phi=-\phi-K/2\gamma} \\ = \frac{L}{2\gamma^2 c} \{1 + K^2/12 + \gamma^2[(\phi + K/2\gamma)^2 + \psi^2]\} + \frac{d}{2\gamma^2 c} \{1 + \gamma^2[(\phi + K/\gamma)^2 + \psi^2]\}. \quad (15)$$

The subscripts indicate the change of variable to be performed in Eqs. (4) and (12). Equations (1), (8), and (14) thus lead to the density

$$\frac{\partial^3 W_\sigma}{\partial \phi \partial \psi \partial \omega} = \frac{q^2 \gamma^2}{\pi^3 \epsilon_0 c} \left( \frac{K - \gamma \phi}{1 + (K - \gamma \phi)^2 + \gamma^2 \psi^2} + \frac{K + \gamma \phi}{1 + (K + \gamma \phi)^2 + \gamma^2 \psi^2} \right)^2 \sin^2\left(\frac{\omega T}{2}\right), \\ \frac{\partial^3 W_\pi}{\partial \phi \partial \psi \partial \omega} = \frac{q^2 \gamma^4 \psi^2}{\pi^3 \epsilon_0 c} \left( \frac{1}{1 + (K - \gamma \phi)^2 + \gamma^2 \psi^2} - \frac{1}{1 + (K + \gamma \phi)^2 + \gamma^2 \psi^2} \right)^2 \sin^2\left(\frac{\omega T}{2}\right). \quad (16)$$

This is schemed in Fig. 3 (drawn earlier as well from numerical simulations ([13], Fig. 6) that has been obtained for 20 GeV electron,  $d = 0.2$  m distant  $L = 0.5$  m long dipoles with, respectively,  $K = \pm 10$ , and observation frequency  $\omega \approx 3.8 \times 10^{15}$  rad/s (visible light); the  $\phi$  asymmetry that shows ensues from the nonsymmetry of  $T(\phi)$  [Eq. (15)]. The first ring in the modulation pattern arises at very large aperture  $\gamma\sqrt{\phi^2 + \psi^2} \approx 30$  [Eq. (15) with  $T = \pi/\omega$ ]; in particular, upon interference the intensity is damped by  $4 \sin^2(\omega T_2) \approx (\omega T)^2$ , corresponding to the region  $|\gamma\phi|, |\gamma\psi| \ll 20$ , well within the first interferential ring; indeed,  $\omega \Delta T$  is supposed to be  $\ll 1$ ,

entailing that  $\omega T \ll 1$  as well, since  $T = \Delta T + \Delta T_d$  while  $\Delta T_d \approx \Delta T$  given that  $d \approx L$ . At LEP edge SR in the  $\phi = K/\gamma > 0$  region was intercepted by the video setup; in these conditions  $T \approx 2K^2 L / 3\gamma^2 c$ , hence a damping of  $(\omega T)^2 \approx 0.08$ , as can be observed in Fig. 3, in fair agreement with measurements [13].

*Comments on the validity of the low frequency model.*— Dipole lengths  $L = 0.5$  m and spacing  $d = 0.2$  m considered here do not actually fulfill the short source hypothesis  $L < d$ , yet numerical simulations [15] prove the low frequency analytical material to still provide good enough precision in that miniwiggler configuration. In addition, one gets the  $\gamma$ -independent limit  $\omega_{\text{limit}} \approx 4c/\alpha^2 L \approx 1.5 \times 10^{16}$  rad/s [after Eq. (5)], about 6 times the observed frequency, entailing negligible approximation error that furthermore concerns far tails of the energy density distribution.

## B. Visible edge SR from GeV range electrons

Edge SR interference with electrons has been subject to numerous experiments and more or less detailed theoretical studies, always based on the strong field approximation (which in practice means very long dipoles; see, for instance, Refs. [9,16]). The present low frequency formalism allows retrieving these results and generalizing to arbitrary strength dipoles.<sup>2</sup>

Figure 4 schemes a typical configuration of interfering edges and defines the straight particle trajectory between the two dipoles as the origin for the observation direction

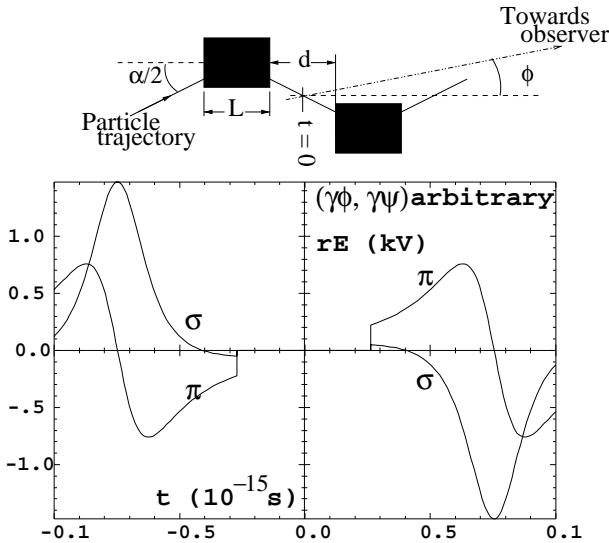


FIG. 2. Top: typical interferential dipole doublet geometry. Bottom: typical shape of the electric field impulse from the two neighboring dipoles [Eq. (14)]. Both polarizations are odd functions of time whatever the observation direction  $(\gamma\phi, \gamma\psi)$ .

<sup>2</sup>Considerations that follow apply as well to TeV range protons [11].

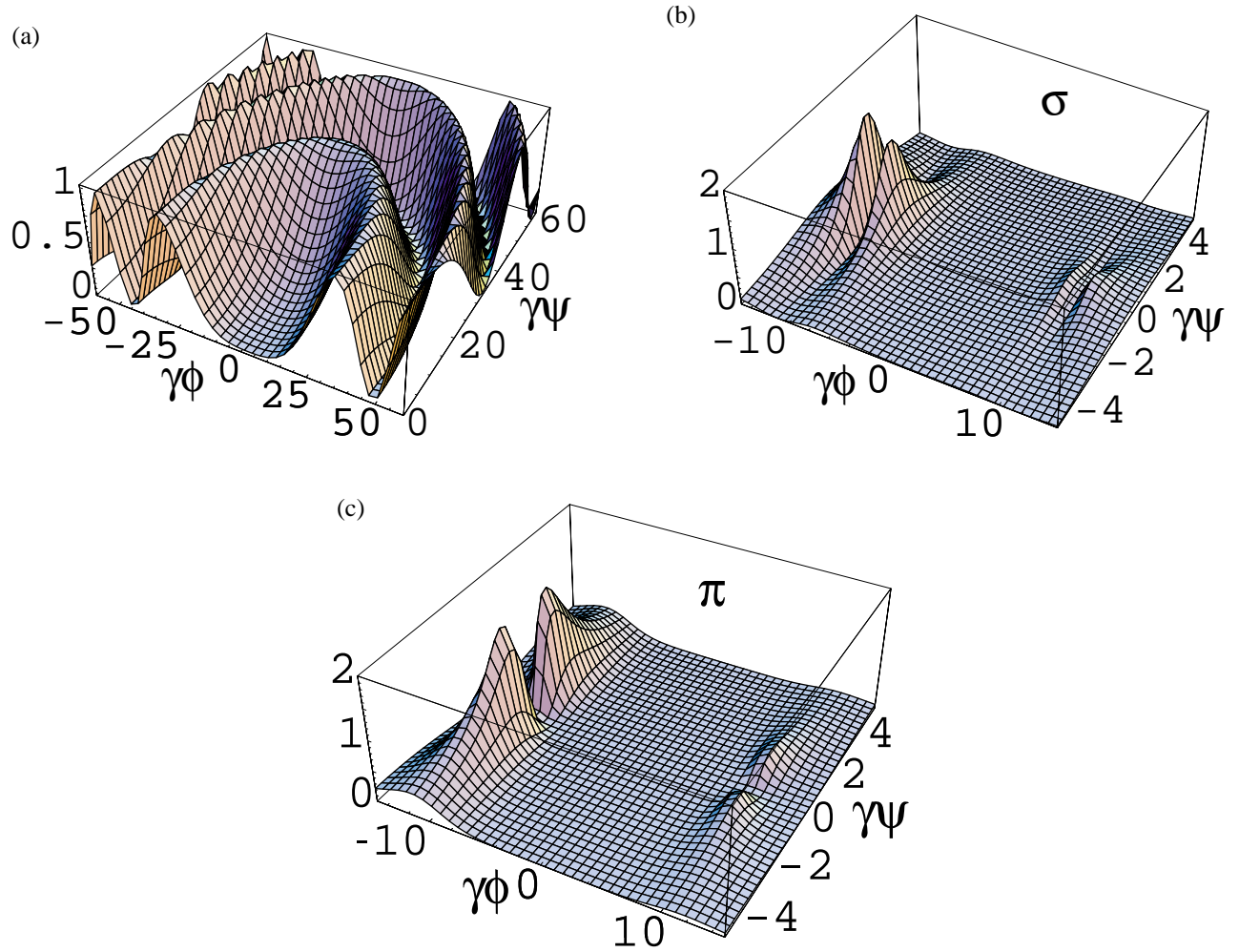


FIG. 3. (Color) Interference between two short dipoles [Eq. (16)]. (a)  $\sin^2(\omega T/2)$  modulation pattern. (b),(c) Resulting  $\sigma$  and  $\pi$  density distributions, normalized as in Fig. 1; the right-hand SR peaks are damped by about 0.08 with respect to the left-hand SR peaks.

angular coordinate  $\varphi$ . Figure 4 also shows typical electric field impulse doublet  ${}^{11}E_{\sigma,\pi}(\varphi, \psi, t) = \delta(t + T/2) * E_{1\sigma,\pi} + \delta(t - T/2) * E_{2\sigma,\pi}$  so generated [Eqs. (7) and (11) with  $N = 2$  and  $T_1 = -T_2 = T/2$ ]. This expression cannot be made simpler because  ${}^{11}E_{\sigma,\pi}(\varphi, \psi, t)$  has no special time symmetry [contrary to Eq. (14), for instance, whose simpler form is due to the electric field impulse series being an odd function of time for all observation angles] unless  $\varphi \rightarrow 0$  in which case  ${}^{11}E_{\sigma}(\psi, t)$  is even and  ${}^{11}E_{\pi}(\psi, t)$  is odd whatever  $\psi$  (this is addressed in the section “Strong field approximation” below). The total du-

ration of the signal is  $\Delta T|_{\phi=\varphi+K/\gamma} + \Delta T_d|_{\theta^2=\varphi^2+\psi^2} + \Delta T|_{\phi=\varphi-K/\gamma}$ , as obtained by combination of Eqs. (4) and (12) with change of variables  $\phi = \varphi \pm K/\gamma$  and  $\theta^2 = \varphi^2 + \psi^2$  according to the frame defined in Fig. 4.

Taking time origins for the single impulses  $E_{1,2}(\varphi, \psi, t)$  at, respectively, the right end of the left dipole and at the left end of the right dipole, the coherence time can be simplified to the traversal of the straight section, namely [Eq. (12)],  $T = \Delta T_d|_{\theta^2=\varphi^2+\psi^2} = d/2\gamma^2 c \times [1 + \gamma^2(\varphi^2 + \psi^2)]$ . This leads to the interference density at observer [Eqs. (1) and (13)]

$$\frac{\partial^3 {}^{11}W_{\sigma,\pi}}{\partial \varphi \partial \psi \partial \omega} = 2\epsilon_0 c r [\tilde{E}_{\sigma,\pi}^2|_{\phi=K/\gamma+\varphi} + \tilde{E}_{\sigma,\pi}^2|_{\phi=-K/\gamma+\varphi} + 2\tilde{E}_{\sigma,\pi}|_{\phi=K/\gamma+\varphi} \tilde{E}_{\sigma,\pi}|_{\phi=-K/\gamma+\varphi} \cos(\omega T)] \quad (17)$$

given [Eq. (8) with change of variables as indicated in subscript]

$$\begin{aligned} \tilde{E}_{\sigma}|_{\phi=\pm K/\gamma+\varphi} &= \frac{q\gamma}{(2\pi)^{3/2}\epsilon_0 c r} \left( \frac{\mp \gamma \varphi}{1 + \gamma^2 \varphi^2 + \gamma^2 \psi^2} + \frac{2K \pm \gamma \varphi}{1 + (2K \pm \gamma \varphi)^2 + \gamma^2 \psi^2} \right), \\ \tilde{E}_{\pi}|_{\phi=\pm K/\gamma+\varphi} &= \frac{q\gamma}{(2\pi)^{3/2}\epsilon_0 c r} \gamma \psi \left( \frac{\pm 1}{1 + \gamma^2 \varphi^2 + \gamma^2 \psi^2} \mp \frac{1}{1 + (2K \pm \gamma \varphi)^2 + \gamma^2 \psi^2} \right). \end{aligned} \quad (18)$$

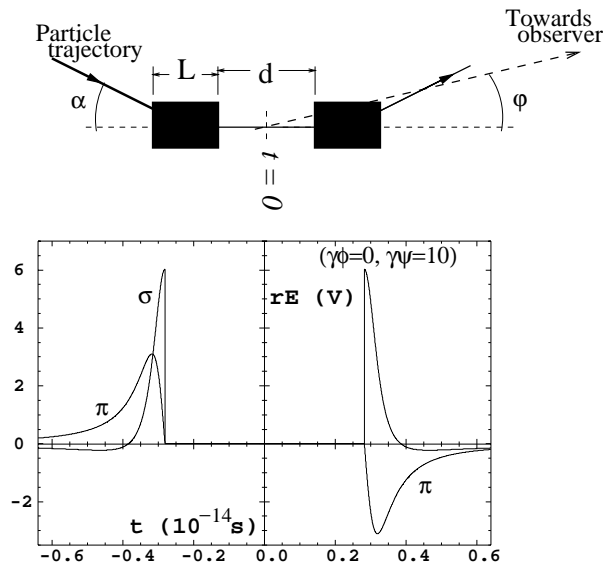


FIG. 4. Top: dipoles with interfering ends. Bottom: typical shape of the electric field; the time symmetry breaks when  $\gamma\varphi \neq 0$ .

Equation (17) is schemed in Fig. 5 obtained by considering 2.5 GeV electrons,  $d = 8$  m distant dipoles with  $K = 10$ , and observation frequency  $\omega = 9.4 \times 10^{14}$  rad/s ( $\lambda = 2 \times 10^{-6}$  m). The interference rings are located at  $\gamma\sqrt{\varphi^2 + \psi^2} \approx 2.23, 4.1$ , etc. It can be observed in Fig. 5 that, contrary to commonly admitted strong field hypothesis ( $K \gg 1$ , see below) the sum density  $\partial^3 W_{\sigma+\pi}/\partial\varphi\partial\psi\partial\omega$ , in general, is not cylindrically symmetric.

From Eq. (5) taken for  $K \approx 1$  that corresponds to the transit time in the end field regions from the observer viewpoint, one gets  $\omega_{\text{limit}} \approx \omega_c/6$ , which means that Eq. (17) is valid up to, for instance, far UV in GeV electron machines and visible light in TeV-range proton machines.

In Appendix B we show the accuracy of the low frequency analytical model from comparison with approximation free numerical simulations, well beyond significant spectral angular energy density levels.

### Strong field approximation (symmetric signal)

The strong field approximation  $K \gg 1$  is the case addressed in earlier publications and concerns interference between neighboring edges of long, high field dipoles [9,16]. This approximation can be drawn in the following way from Eq. (17) that holds instead for arbitrary values of the deflection parameter  $K$  [and hence for arbitrarily weak or short dipoles, in contrast to Eq. (20)].

After Eq. (17) the angular density takes its largest values within  $\gamma\sqrt{\varphi^2 + \psi^2} = a$  few times ( $1/\gamma$ ) so that strong dipole edge SR ( $K \gg 1$ ) is concerned with ranges  $|\gamma\varphi|, |\gamma\psi| \ll K$ , entailing that  $\gamma\varphi$  can be neglected with respect to  $K$  in Eq. (18) (in the time domain it means

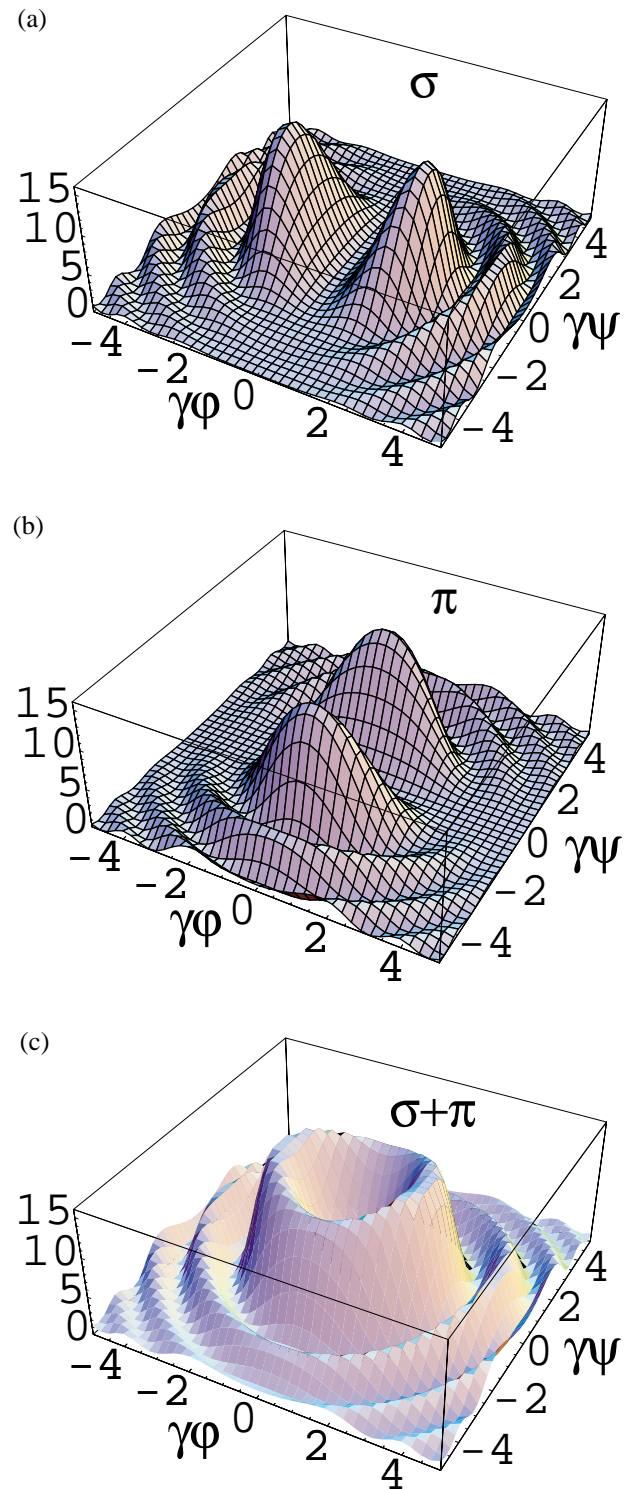


FIG. 5. (Color) Low frequency distributions from interfering dipole edges [Eq. (17)], normalized as in Fig. 1. The low frequency model reveals that the  $\sigma + \pi$  density is not cylindrically symmetric, contrary to the strong field approximation [Eq. (20)].

that the symmetry observed in the electric field impulse schemed in Fig. 4 is preserved over a  $\gamma\varphi$  range of several units). Doing so leads to

$$\begin{aligned}\tilde{E}_{S,\sigma}(\phi, \psi, \omega)|_{\phi=\pm K/\gamma+\varphi} &\approx \frac{q\gamma}{(2\pi)^{3/2}\epsilon_0 c r} \left( \frac{\mp\gamma\varphi}{1+\gamma^2(\varphi^2+\psi^2)} + \frac{2K}{1+4K^2+\gamma^2\psi^2} \right), \\ \tilde{E}_{S,\pi}(\phi, \psi, \omega)|_{\phi=\pm K/\gamma+\varphi} &\approx (\pm) \frac{q\gamma}{(2\pi)^{3/2}\epsilon_0 c r} \gamma\psi \left( \frac{1}{1+\gamma^2(\varphi^2+\psi^2)} - \frac{1}{1+4K^2+\gamma^2\psi^2} \right),\end{aligned}\quad (19)$$

where the upper sign is for the right end of the left dipole, the lower sign is for the left end of the right dipole, and the index  $S$  stands for the strong field approximation. The rightmost  $\varphi$ -independent term in  $\tilde{E}_{S,\sigma}$  contributes significantly only in regions  $\gamma\varphi \ll 1$  that, however, encompass negligible intensity (compared to emission at  $\gamma\varphi \approx 2$ ; see Fig. 5). In addition, calculation shows that upon inter-

ference it contributes a  $\cos^2(\omega T/2)$  modulation term for all  $\gamma\varphi$  negligible as well so long as  $\omega T \not\rightarrow 2k\pi$  ( $k \in \mathbb{N}$ ). Therefore, on the one hand, one ends up with a simplified form of Eq. (13),  ${}^{11}\tilde{E}_{S,\sigma,\pi}(\varphi, \psi, \omega) = \mp(e^{i\omega T/2} - e^{-i\omega T/2})\tilde{E}_{\sigma,\pi}(\phi, \psi, \omega)|_{\phi=K/\gamma+\varphi}$ , and, on the other hand, as a consequence Eq. (17) reduces to (with the expected simple  $\sin^2$  modulation due to the  $\varphi$  symmetry of the signal, as in Sec. III A)

$$\begin{aligned}\frac{\partial^3 {}^{11}W_{S,\sigma}}{\partial\varphi\partial\psi\partial\omega} &\approx \frac{q^2\gamma^2}{2\pi^3\epsilon_0 c} \left( \frac{\gamma\varphi}{1+\gamma^2(\varphi^2+\psi^2)} \right)^2 \sin^2\left(\frac{\omega T}{2}\right), \\ \frac{\partial^3 {}^{11}W_{S,\pi}}{\partial\varphi\partial\psi\partial\omega} &\approx \frac{q^2\gamma^2}{2\pi^3\epsilon_0 c} \left( \frac{\gamma\psi}{1+\gamma^2(\varphi^2+\psi^2)} \right)^2 \sin^2\left(\frac{\omega T}{2}\right) \quad (K \gg 1, \gamma\varphi \not\rightarrow 0),\end{aligned}\quad (20)$$

where, in addition, the  $K$ -dependent factor in  $\tilde{E}_{S,\pi}$  [Eq. (19)] has been neglected since  $4K^2 \gg 1 + \gamma^2(\varphi^2 + \psi^2)$  as stressed above; note that by eliminating the  $\cos^2(\omega T/2)$  term one gets  $\partial^3 {}^{11}W_{S,\sigma}/\partial\varphi\partial\psi\partial\omega \xrightarrow{\omega \rightarrow 0} 0$ , which is obviously nonsense since  $\int E_\sigma(\varphi, \psi, t) dt \neq 0$  as can be checked in Fig. 4, which further restrains the validity of Eq. (20) to “not too small”  $\omega$  values. Besides, Eq. (20) has the same form as Eq. (16) due to  ${}^{11}E_\sigma(t)$  and  ${}^{11}E_\pi(t)$  being, respectively, even and odd functions of time whatever  $\varphi, \psi$  in the strong field approximation, as pointed out above (Fig. 4). Eventually, as expected, the total density  $\frac{\partial^3 {}^{11}W_{S,\sigma+\pi}}{\partial\varphi\partial\psi\partial\omega} = \frac{q^2\gamma^2}{2\pi^3\epsilon_0 c} \left( \frac{\gamma^2(\varphi^2+\psi^2)}{1+\gamma^2(\varphi^2+\psi^2)} \right)^2 \sin^2\left(\frac{\omega T}{2}\right)$  has cylindrical symmetry.

### C. Infrared SR from a three-dipole wiggler, isolated $2/\gamma$ kick

Implications of the low frequency hypothesis on wiggler SR have been discussed recently [16]. We derive additional properties from the analytical formalism above. We show how a specially tailored closed orbit geometry allows isolating the highest brightness infrared SR source that a  $2/\gamma$  kick provides [6].

We consider a three-dipole wiggler based on a central  $(2/\gamma)$ -deviation magnet ( $|K| = 1$  in the central dipole and  $|K| = 0.5$  in the end dipoles) which, in particular, allows showing the dramatic interference induced damping in the low frequency range.

The low frequency limit now writes  $\omega_{\text{limit}} \approx \omega_c/6$  leading for instance to validity range  $\omega < 4 \times 10^{16}$  rad/s ( $\lambda > 40 \times 10^{-9}$  m) for a 2.5 GeV electron traversing a, e.g., 670 kG,  $L = 5 \times 10^{-2}$  m long dipole. Figure 6 shows the wiggler geometry and the typical electric field impulse series so generated [Eqs. (7) and (11)] with  $N = 3$  and using coherence times as given in Eq. (21); its total duration is

$$\begin{aligned}\Delta T|_{L/2, K/2, \phi=\varphi-K/2\gamma} + \Delta T_d|_{\theta^2=(\varphi-K/\gamma)^2+\psi^2} \\ + \Delta T|_{\phi=\varphi} + \Delta T_d|_{\theta^2=(\varphi+K/\gamma)^2+\psi^2} \\ + \Delta T|_{L/2, K/2, \phi=\varphi+K/2\gamma}.\end{aligned}$$

Note that the time symmetry observed in the figure is due to  $\gamma\varphi = 0$  and breaks otherwise (the various impulses evolve in nonsymmetric ways).

The origins of  $\varphi$  angle and time being taken at the center of the central dipole, the coherence times in Eq. (11) write  $T_2 = 0$  and [Eqs. (4) and (12)]

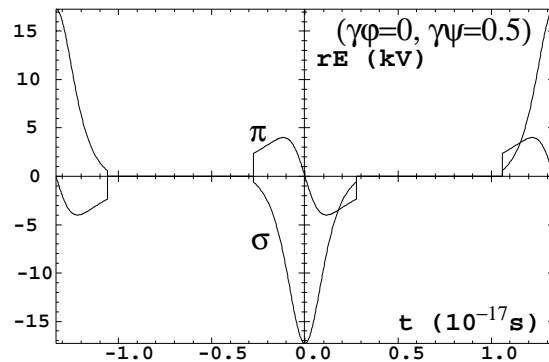
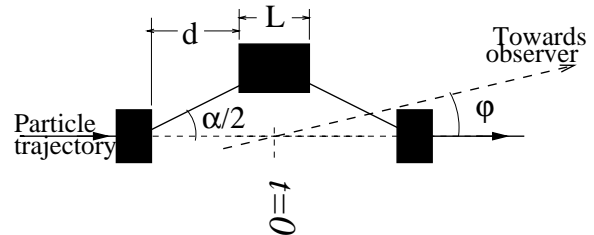


FIG. 6. Top: a three-dipole wiggler. Bottom: typical shape of the electric field impulse in the  $\gamma\varphi = 0$  observation direction. Note that the central impulse can be obtained from Eq. (7) with  $\phi = 0$  and the side impulses with  $\phi = \pm\alpha/2$ .

$$\begin{aligned}
-T_1 &= \Delta T|_{L/2, K/2, \phi=\varphi-K/2\gamma} + \Delta T_d|_{\theta^2=(\varphi-K/\gamma)^2+\psi^2} + \frac{1}{2} \Delta T|_{\phi=\varphi} \\
&= \frac{L/2}{2\gamma^2 c} \{1 + (K/2)^2/3 + \gamma^2[(\varphi - K/2\gamma)^2 + \psi^2]\} + \frac{d}{2\gamma^2 c} [1 + \gamma^2(\varphi - K/\gamma)^2 + \psi^2] \\
&\quad + \frac{1}{2} \frac{L}{2\gamma^2 c} [1 + K^2/3 + \gamma^2(\varphi^2 + \psi^2)] \\
+T_3 &= \frac{1}{2} \Delta T|_{\phi=\varphi} + \Delta T_d|_{\theta^2=(\varphi+K/\gamma)^2+\psi^2} + \Delta T|_{L/2, K/2, \phi=\varphi+K/2\gamma} \\
&= \frac{1}{2} \frac{L}{2\gamma^2 c} [1 + K^2/3 + \gamma^2(\varphi^2 + \psi^2)] + \frac{d}{2\gamma^2 c} [1 + \gamma^2(\varphi + K/\gamma)^2 + \psi^2] \\
&\quad + \frac{L/2}{2\gamma^2 c} \{1 + (K/2)^2/3 + \gamma^2[(\varphi + K/2\gamma)^2 + \psi^2]\}.
\end{aligned} \tag{21}$$

Equations (1) and (13) squared, with  $N = 3$ , provide the interferential patterns

$$\frac{\partial^3 W_{\sigma, \pi}}{\partial \varphi \partial \psi \partial \omega} = 2\epsilon_0 c r \{ [\tilde{E}_{\sigma, \pi}|_{K/2, \phi=\varphi-K/2\gamma} \cos(\omega T_1) + \tilde{E}_{\sigma, \pi}|_{-K, \phi=\varphi} + \tilde{E}_{\sigma, \pi}|_{K/2, \phi=\varphi+K/2\gamma} \cos(\omega T_3)]^2 + (ST)^2 \} \tag{22}$$

where (ST) designates the complementary sin term, and given [Eq. (8) with change of variables as indicated in subscript]

$$\begin{aligned}
\tilde{E}_{\sigma}(\phi, \psi, \omega)|_{K/2, \phi=\varphi \pm K/2\gamma} &= \frac{q\gamma}{(2\pi)^{3/2} \epsilon_0 c r} \left( \frac{\mp \gamma \varphi}{1 + \gamma^2 \varphi^2 + \gamma^2 \psi^2} + \frac{K \pm \gamma \varphi}{1 + (K \pm \gamma \varphi)^2 + \gamma^2 \psi^2} \right), \\
\tilde{E}_{\pi}(\phi, \psi, \omega)|_{K/2, \phi=\varphi \pm K/2\gamma} &= \frac{q\gamma}{(2\pi)^{3/2} \epsilon_0 c r} \gamma \psi \left( \frac{\pm 1}{1 + \gamma^2 \varphi^2 + \gamma^2 \psi^2} \mp \frac{1}{1 + (K \pm \gamma \varphi)^2 + \gamma^2 \psi^2} \right), \\
\tilde{E}_{\sigma}(\phi, \psi, \omega)|_{-K, \phi=\varphi} &= -\frac{q\gamma}{(2\pi)^{3/2} \epsilon_0 c r} \left( \frac{K + \gamma \varphi}{1 + (K + \gamma \varphi)^2 + \gamma^2 \psi^2} + \frac{K - \gamma \varphi}{1 + (K - \gamma \varphi)^2 + \gamma^2 \psi^2} \right), \\
\tilde{E}_{\pi}(\phi, \psi, \omega)|_{-K, \phi=\varphi} &= \frac{q\gamma}{(2\pi)^{3/2} \epsilon_0 c r} \gamma \psi \left( \frac{1}{1 + (K + \gamma \varphi)^2 + \gamma^2 \psi^2} + \frac{1}{1 + (K - \gamma \varphi)^2 + \gamma^2 \psi^2} \right).
\end{aligned}$$

This is illustrated in Fig. 7, obtained with dipoles distant  $d = 1$  m and observation frequency  $\omega = 1.9 \times 10^{15}$  rad/s ( $\lambda = 10^{-6}$  m). Comparison with radiation from the central  $2/\gamma$  deviation dipole alone reveals a strong damping of about 0.04 due to the interference. This also appears clearly in Fig. 8 that displays radiation spectra from the wiggler [Eq. (22)], from a single  $K = 1$  dipole [Eq. (9)], and from the body of a very long dipole (the classical  $K_{2/3}^2$  spectrum).

Appendix B shows the accuracy of the analytical material above, well beyond significant spectral angular energy density levels, from comparisons with approximation free numerical simulations.

### Isolated $2/\gamma$ kick

The way to overcome the destructive interference above is to, on the one hand, set the  $(2/\gamma)$  kick in the vertical plane and, on the other hand, tailor on both sides of it a strictly straight orbit as schemed in Fig. 9 [17] (all quadrupoles within the orbit bump comprise vertical corrector circuits tuned so as to cancel the kick that would

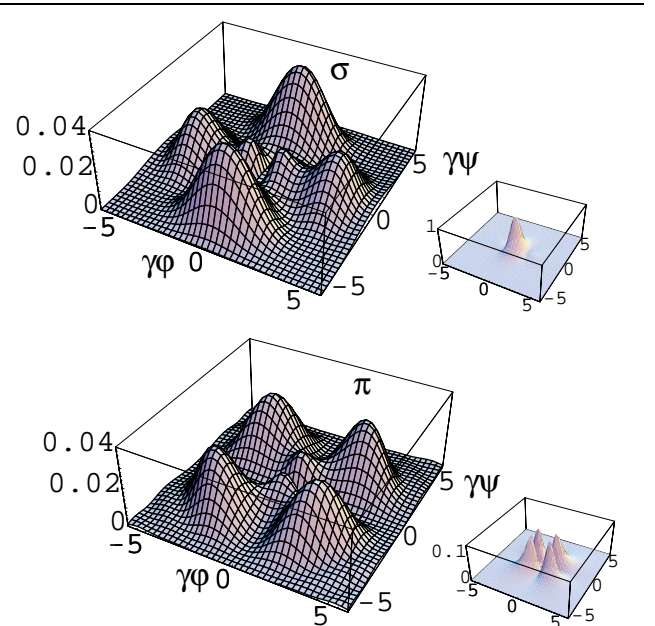


FIG. 7. (Color) Low frequency density distributions from three-dipole wiggler [Eq. (22)]. The small boxes show the energy density from the central dipole alone, for comparison.

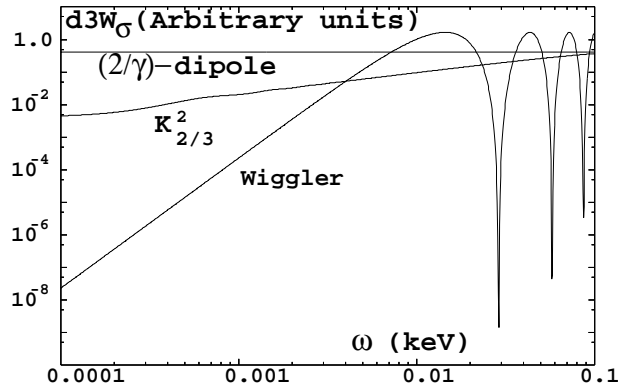


FIG. 8. Interferential spectrum of the wiggler  $\sigma$  component in the forward direction [Eq. (22) with  $\varphi = \psi = 0$ ], together with, for comparison, spectra from the central  $(2/\gamma)$  deviation dipole alone [Eq. (9) with  $K = 1$ ], and from the center of strong dipole [classical  $K^2_{2/3}(\omega)$  shape [8]].

otherwise arise from the off-axis orbit, so that the radiation balance within the quadrupole is null). The vertical bump culminates at the  $(2/\gamma)$  dipole whereas no horizontal closed orbit is excited. In such a configuration, the only remaining SR sources, from the viewpoint of an observer located at the right, are the central  $(2/\gamma)$  dipole, the upstream main bend right edge, and the downstream main bend left edge. It ensues that the vertical (horizontal) interferential polarization component builds up from the  $\sigma$  ( $\pi$ ) component of the  $(2/\gamma)$  dipole plus the  $\pi$  ( $\sigma$ ) components of the main bend edges; given that the bend  $\pi$  components are zero for  $(\varphi, \psi) = (0, 0)$ , the energy density of the  $(2/\gamma)$  kick  $\sigma$  component is therefore fully preserved in that direction (with spectrum as schemed in Fig. 8, single dipole case). The resulting angular densities have been obtained from Eq. (22) (Fig. 10).

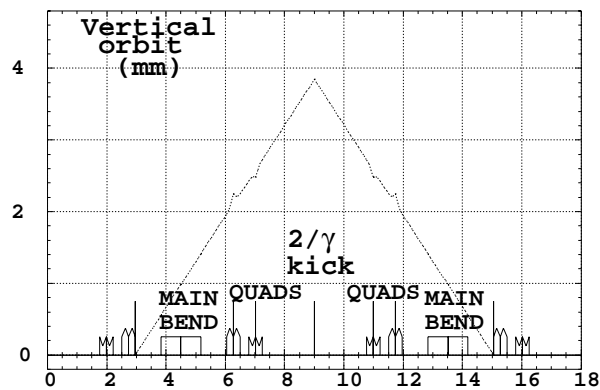


FIG. 9. Vertical triangular orbit bump straddling a typical synchrotron cell.

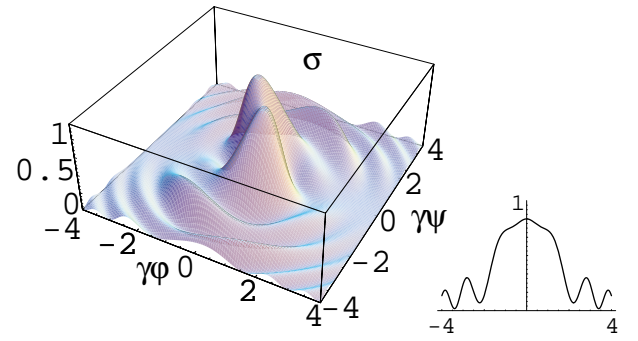


FIG. 10. (Color) Interferential vertical polarization component from the so-tailored “edge- $(2/\gamma)$ -dipole-edge” wiggler  $\lambda = 10^{-6}$  m), and (right plot) a  $\gamma\phi$  cross section of it at  $\gamma\psi = 0$ . Comparison with the single dipole radiation (second plot in Fig. 7) shows that the forward density of the  $(2/\gamma)$  dipole is fully preserved.

#### IV. CONCLUSION

A methodical technique for calculating spectral angular distributions radiated by interfering short SR sources in the low frequency regime is described. It is applied for illustration to three cases where it reveals new features and proves to bring more thorough insight compared to earlier publications: (i) SR interference in the visible range in a typical short dipole interference experiment held at LEP, (ii) a generalization of edge SR interference equations until now restricted to strong neighboring dipoles, (iii) a thorough study of low frequency wiggler radiation and its possible application as an isolated  $2/\gamma$  deviation short dipole used as a highest brightness infrared SR source.

The material presented can serve as an efficient tool for the design and quick optimization of short dipoles or wiggler assemblies dedicated to diagnostics in lepton and TeV range hadron machines. It can further be used for faster calculation (compared to numerical methods) of Fraunhofer diffraction patterns, a mandatory stage in the design of SR based beam cross-section imaging [3,18].

#### ACKNOWLEDGMENTS

We thank Professor R. Coisson, Università di Parma, Italy, and A. Hofmann, CERN, for reading the manuscript and offering encouraging comments.

#### APPENDIX A: CALCULATION OF COHERENCE TIME

We derive here some of the expressions used in the main text regarding the duration of the electric field impulse and coherence times at the observer.

*Single dipole.*—The duration  $\delta T$  of the signal emitted over a trajectory arc of arbitrary extent  $\omega_0 \delta T^l$  is given by

$$2\gamma^2 \int_{\delta T} dt = \int_{\delta T'} [1 + \gamma^2(\phi^2 + \psi^2) - 2\gamma^2\phi\omega_0 t' + \gamma^2\omega_0^2 t'^2] dt'.$$

By integration, and taking coinciding time origins for  $t$  (observer time) and  $t'$  (particle time), we get quantities that intervene in the various examples in the paper, namely, the duration  $T^-$  ( $T^+$ ) of the signal emitted by the particle at the traversal of the first (second) half of the dipole, that satisfy

$$2\gamma^2 c T^\pm = \frac{L}{2} \{1 + \gamma^2[(\phi \mp K/2\gamma)^2 + \psi^2] + K^2/12\}.$$

An outcome is the duration  $\Delta T = T^- + T^+$  of the signal emitted over the all trajectory arc  $\pm\alpha/2$  [Eq. (4)].

*A pair of dipoles of opposite signs.*—In each dipole the particle time origin  $t' = 0$  is taken at the mid-deviation, as previously. Index 1 is for the first dipole, index 2 for the second dipole (as schemed, for instance, in Fig. 2). As to the first dipole, the duration of the signal generated along the arc extending from the time origin down to its exit ( $0 < \omega_0 t' < \alpha/2$ ) is  $2\gamma^2 c T_1^+ = \frac{L_1}{2} \{1 + \gamma^2[(\phi_1 - K_1/2\gamma)^2 + \psi^2] + K_1^2/12\}$ . As to the second dipole, the duration of the signal from the dipole entrance down to its time origin ( $-\alpha/2 < \omega_0 t' < 0$ ) is  $2\gamma^2 c T_2^- = \frac{L_2}{2} \{1 + \gamma^2[(\phi_2 + K_2/2\gamma)^2 + \psi^2] + K_2^2/12\}$ . Considering dipoles that differ only by their curvature sign, we note  $L_1 = L_2 = L$ ,  $\alpha_1 = \alpha_2 = \alpha$ . In addition,  $\phi_1 \equiv -\phi$  and  $\phi_2 \equiv \phi$  in the frame as defined in Figs. 2 and 6. This leads to

$$\begin{aligned} 2\gamma^2 c T_1^+ &= 2\gamma^2 c T_2^- \\ &= \frac{L}{2} \{1 + \gamma^2[(\phi + K/2\gamma)^2 + \psi^2] + K^2/12\}. \end{aligned}$$

Given the change of variables indicated in subscript this can be rewritten under the form [as, for instance, in Eqs. (15) and (21)]

$$2\gamma^2 c T_1^+ = 2\gamma^2 c T_2^- = \Delta T|_{K=K/2, \phi=\phi+K/2\gamma}.$$

## APPENDIX B: COMPARISON WITH NUMERICAL SIMULATIONS

Numerical tools have been developed based on the exact Fourier transform of the electric field impulse as obtained from ray tracing [15,19]. They are applied to the examples of Secs. III B and III C for checking the accuracy and possible validity limit of the low frequency analytical formalism. Comments are provided in the captions of Fig. 11 as to edge SR and Fig. 12 as to wiggler SR.

## APPENDIX C: HIGHER ORDER LOW FREQUENCY APPROXIMATION

In LHC at collision energy (7 TeV proton beams), the use of synchrotron radiation emitted by a miniwiggler is envisaged for the measurement of beam emittances [10]. The miniwiggler is composed of four 1 m long superconducting magnets with 6 T maximum magnetic field.

Figure 13 illustrates the good behavior of the low frequency SR model in the single dipole case. However, the geometrical configuration and proton energy of concern

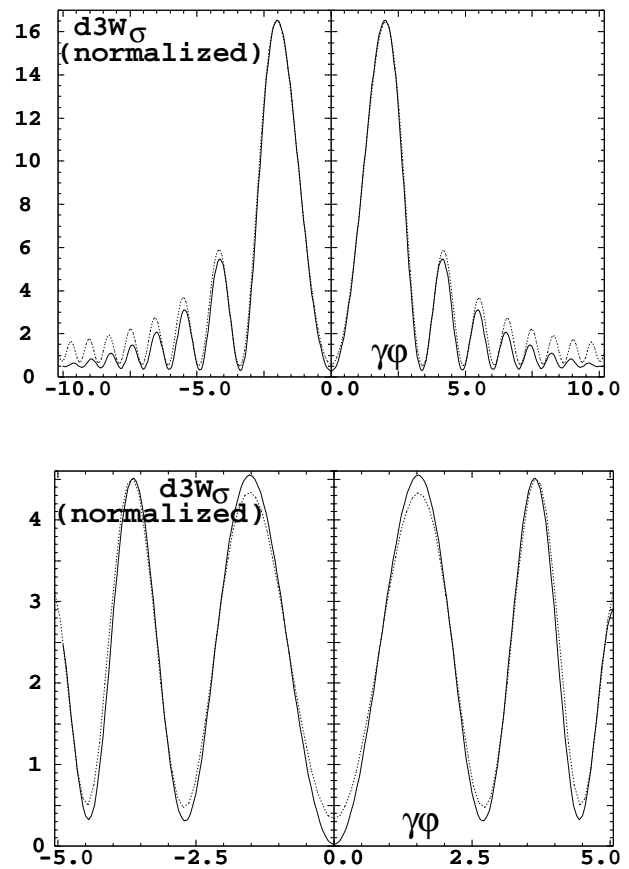


FIG. 11. Edge-edge low frequency SR (section views of Fig. 5). Top:  $\partial^3 W_\sigma / \partial \omega \partial \phi \partial \psi$  vs  $\gamma\phi$  at  $\gamma\psi = 0$ . Bottom:  $\partial^3 W_\sigma / \partial \omega \partial \phi \partial \psi$  vs  $\gamma\phi$  at  $\gamma\psi = 2$ . Solid curves are from Eq. (17), dashed curves are from numerical simulations. The agreement remains good far beyond the rms aperture in spite of observation wavelength  $\lambda = 2 \times 10^{-6}$  m slightly shorter than  $\lambda_{\text{limit}} = 4\pi\rho K(1 + K^2)/\gamma^3 \approx 5 \times 10^{-6}$  m (given  $\rho \approx 50$  m in this example). Such short wavelength was chosen on purpose to show the fair behavior of the low frequency formalism up to the region of frequency validity limit; this is due to the slow decay of the spectral energy density when  $\omega > \omega_{\text{limit}}$ . Similar agreement is observed for the  $\pi$  component, not shown here.

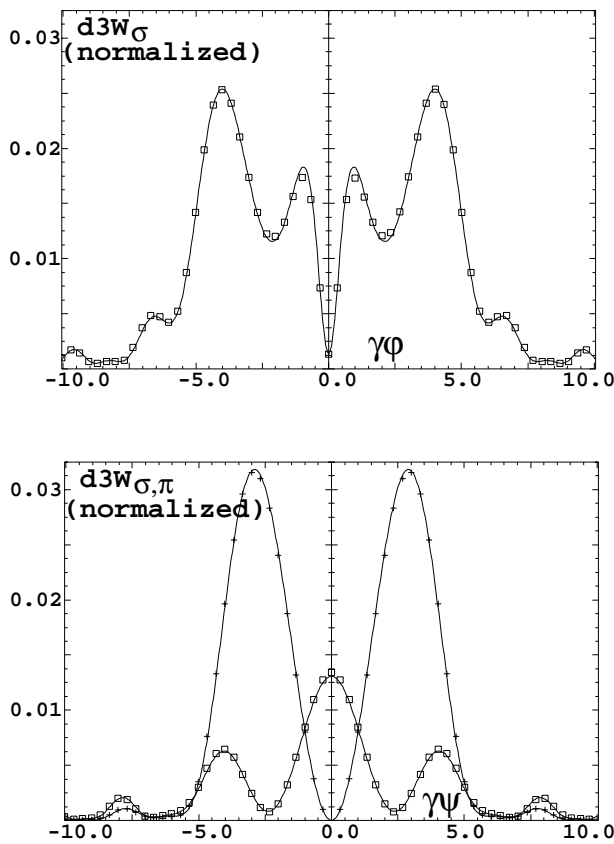


FIG. 12. Wiggler low frequency SR (section views of Fig. 7). Top:  $\partial^3 W_\sigma / \partial \omega \partial \phi \partial \psi$  vs  $\gamma\phi$  at  $\gamma\psi = 0$ . Bottom:  $\partial^3 W_{\sigma,\pi} / \partial \omega \partial \phi \partial \psi$  vs  $\gamma\phi$  at  $\gamma\psi = 2.5$ . Solid lines are from Eq. (22) while squares ( $\sigma$  component) and crosses ( $\pi$  component) are from numerical simulations. Here  $\omega \ll \omega_{\text{limit}}$ . The excellent behavior of the low frequency SR formalism up to large  $(\phi, \psi)$  ranges well beyond significant energy density levels is evident.

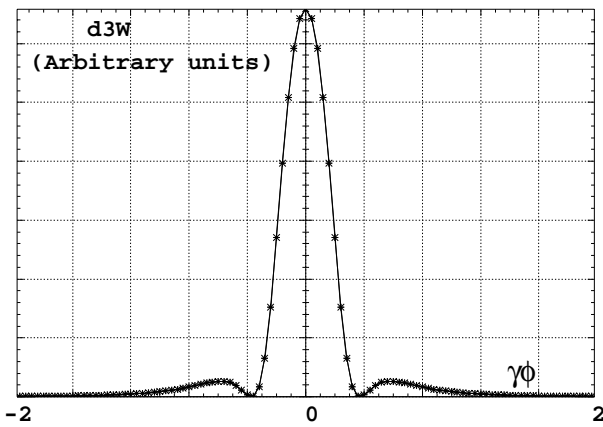


FIG. 13.  $\partial^3 W_\sigma / \partial \omega \partial \phi \partial \psi$  vs  $\gamma\phi$  at  $\psi = 0$ , for  $\omega = 1.13$  eV. The solid curve is from numerical simulation, and the crosses are from Eq. (9).

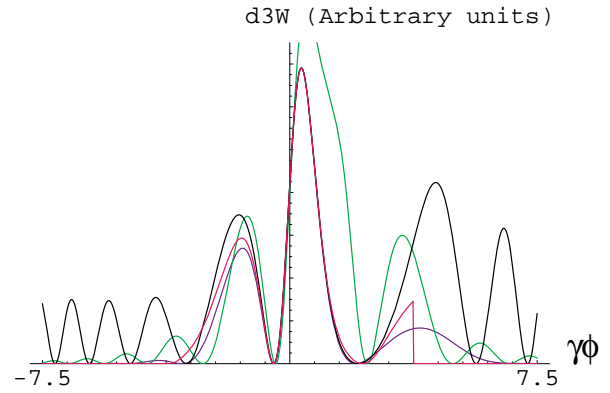


FIG. 14. (Color)  $\partial^3 W_\sigma / \partial \omega \partial \phi \partial \psi$  vs  $\gamma\phi$  at  $\psi = 0$ , for two dipoles distant 0.5 m. The blue curve is the exact Fourier transform, the green curve is the low frequency model [Eq. (16)], the black curve is the first order  $\omega$  approximation [in Eq. (2)], and the red curve is the second order.

lead to single signal duration of the same order of magnitude as the time interval between two dipoles, which requires higher order expansion of Eq. (2), basically up to second order in  $\omega$  to get precise enough  $\phi, \psi$  angular distributions over an aperture of a few times  $1/\gamma$ , as shown in Fig. 14 in the case of an interfering dipole pair [11].

- [1] M. M. Nikitin, A. F. Medvedev, M. B. Moiseev, and V. Ya Épp, *Sov. Phys. JETP* **52**, 388–394 (1980).
- [2] J. Bosser, L. Burnod, R. Coisson, G. Ferioli, J. Mann, and F. Méot, *J. Phys. (Paris), Lett.* **45**, 343–351 (1984).
- [3] A. Hofmann, in *Proceedings of the CERN Accelerator School, Grenoble, 1996* (CERN, Geneva, 1998).
- [4] J. Bosser, C. Bovet, and R. Jung, CERN LHC/Note No. 192, 1992.
- [5] J.-L. Laclare, M.-P. Level, and P. Roy, in *Proceedings of the Workshop on Infrared SR, Gif-sur-Yvette, 1997* (LURE, Orsay, 1998).
- [6] F. Méot, *Part. Accel.* **62**, 215–239 (1999).
- [7] F. Méot and N. Ponthieu, CEA/Saclay Report No. DSM/DAPNIA/SEA-98-53, 1998.
- [8] A. Hofmann, in *Proceedings of the CERN Accelerator School, Grenoble, 1996* (Ref. [3]).
- [9] O. Chubar, Kurtchatov Institute Report No. IAE-5596/14, 1992.
- [10] L. Cadet, in *Proceedings of the 1st CERN LHC Emittance Workshop, Geneva, 2000*, <http://emittanceworkshop.web.cern.ch/EmittanceWorkshop>.
- [11] L. Ponce, CERN SL/BI-PM internal report (to be published).
- [12] E. Rossa, F. Tecker, and J. C. Mathae, in *Proceedings of the Particle Accelerator Conference, Washington, D.C., 1993* (IEEE, Piscataway, NJ, 1993).
- [13] C. Bovet, A. Burns, F. Méot, M. Placidi, E. Rossa, and J. de Vries, CERN Report No. CERN SL/97-59 (BI), 1997; in *Proceedings of the Particle Accelerator Conference, Vancouver, Canada, 1997* (IEEE, Piscataway, NJ, 1998).

- [14] K. Hanke, Report No. PITHA 94/1, RWTH, CERN SL/Note No. 95-65 (BI), 13/06/1995; A. J. Burns, CERN SL/Note No. 96-53 (BI), CERN, 21/08/96.
- [15] F. Méot, CERN Report No. CERN SL/94-22 (AP), 1994.
- [16] R. A. Bosch, Nucl. Instrum. Methods Phys. Res., Sect. A **386**, 525–530 (1997).
- [17] F. Méot, CEA Saclay and LURE Orsay, internal note, 1998.
- [18] A. Hofmann and F. Méot, Nucl. Instrum. Methods Phys. Res., Sect. A **203**, 483–493 (1982).
- [19] Numerical simulations proceed from trajectory tracing, from which the radiated electric field  $\vec{E}(t) = (q/4\pi\epsilon_0 c)\vec{n}(t') \times \{[\vec{n}(t') - \vec{\beta}(t')] \times \dot{\vec{\beta}}(t')\} / r(t') \times [1 - \vec{n}(t') \cdot \vec{\beta}(t')]^3$  is calculated numerically and then Fourier transformed numerically as well (see Ref. [15]); F. Méot and S. Valero, Nucl. Instrum. Methods Phys. Res., Sect. A **427**, 353–356 (1993).